

## NUMERICAL SIMULATION OF THE CASTING PROCESS OF AN AZ91D MAGNESIUM ALLOY UNDER A ROTATING-PULSED COMBINED ELECTROMAGNETIC FIELD

Z. Liang <sup>a</sup>, Q.-W. Bai <sup>abc\*</sup>, Y.-C. Tian <sup>d</sup>, Y. Liu <sup>a</sup>, K.-H. Zhang <sup>a</sup>, H.-M. Lai <sup>a</sup>

<sup>a</sup> School of Rare Earth Industry, Inner Mongolia University of Science and Technology, Baotou, China

<sup>b</sup> Key Laboratory of Green Extraction & Efficient Utilization of Light Rare-Earth Resources (Inner Mongolia University of Science and Technology), Ministry of Education, Baotou, China

<sup>c</sup> Inner Mongolia Autonomous Region Carbon Neutrality Collaborative Innovation Center

<sup>d</sup> Inner Mongolia Institute of Metal Materials, Baotou, P. R. China.

(Received 20 December 2023; Accepted 27 August 2024)

### Abstract

Using an AZ91D magnesium alloy as the research object, a three-dimensional (3D) numerical model was created and simulated using simulation analysis software. The effects of a rotating electromagnetic field (REMF), a pulsed electromagnetic field (PEMF) and a rotating pulsed electromagnetic field (R-PEMF) on the magnetic field and the flow field of a metal melt were investigated. The simulation results show that during the REMF treatment a rotational force is generated on the cross-section of the melt, and the PEMF exerts a magnetic pressure on the cross-section of the melt. Under the combined effect of these two forces, the Lorentz force increases parallel to the melt axis, and a secondary flow directed towards the core of the melt is generated, which contributes to the homogenization of the melt. By analyzing the solidification structure and elemental distribution of the metal, R-PEMF was shown to effectively improve the solidification structure and macrosegregation of Al in AZ91D magnesium alloy.

**Keywords:** Pulsed electromagnetic field; Rotating electromagnetic field; Combined electromagnetic field; Magnesium alloy; Numerical simulation

### 1. Introduction

Magnesium alloys are the lightest engineering structural metal material at present. Because of their low density, high specific strength, high specific stiffness, good thermal conductivity, electromagnetic interference shielding performance, good cutting performance and good casting performance, magnesium alloys are considered to have broad application prospects in aerospace, automotive lightweight, electronic 3C, biomedical and energy fields. In terms of environmental friendliness, magnesium alloy waste can be recycled and reused; this process is known as “green engineering new material in the 21st century” [1-7]. However, due to the high chemical activity of magnesium, the corrosion resistance of magnesium alloys is poor. Due to the small heat capacity and large solidification range of cast magnesium alloys, composition segregation can easily occur during solidification or casting, and these alloys often contain casting defects

such as holes and inclusions after casting [8,9]. Second, the specific gravity segregation in the casting of rare earth magnesium alloys leads to the inhomogeneity of rare earth elements in the alloy, which leads to the inhomogeneity of the properties of rare earth magnesium alloys [10,11]. These issues have limited the production and application of magnesium alloys. Researchers are exploring ways to improve the corrosion resistance of magnesium alloys through microalloying and different aging treatments [12,13]. For other casting defects, it is currently common to refine the grains of magnesium alloys by adding grain refining agents and stirring methods to reduce these defects; however, these refinements generally increase the cost, and they also pollute the melt itself [2,14]. Therefore, improving the performance of conventional magnesium alloy components is worthy of study. At present, the commonly used methods are ultrasonic vibration treatment or mechanical stirring treatment. Ultrasonic vibration and mechanical stirring equipment are in

Corresponding author: [abcqingwei@imust.edu.cn](mailto:abcqingwei@imust.edu.cn)

<https://doi.org/10.2298/JMMB231220016L>



direct contact with the melt, which easily exacerbates the oxidation of magnesium alloys and often results in impurities that can form unknown structures and phases. Moreover, when using the ultrasonic vibration method, the refining effect is not uniform because the vibration intensity decreases rapidly as the distance from the transmitter increases [15].

REMF and PEMF have significant effects on the homogenization treatment of light metal alloys, but there are differences in the form and mechanism of the Lorentz force. In terms of grain refinement, S.Y. Gao et al. reported that REMF had a good grain refinement effect on Mg alloys [16]. The flush effect caused by the forced convection of the melt during the REMF treatment process and the Joule heat generated by the current destroy, crush or fuse the dendrite arms during the solidification process. The broken dendrites can act as the core of new grains to increase the nucleation rate [17]. Although PEMF is used to refine the grains of magnesium alloys, it also has certain negative effects; for example, J.W. Fu reported that a large number of shrinkage pores appeared when treating magnesium alloys with PEMF [18]. In terms of element segregation, element segregation occurs during traditional magnesium alloy casting, which leads to high enrichment of the alloying elements Al and Zn on the surface of the billet and depletion in the center of the billet. Moreover, Griffiths et al. reported that REMF exacerbated the macroscopic segregation of this element in magnesium alloys [19]. However, Zhang Cheng et al. found by means of experiments and simulations that melt under the action of a PEMF with suitable parameters generated forced flow to promote melt exchange in the center and sides of the melt [20]. The macrosegregation in the billet is thus reduced, resulting in a more uniform distribution of alloying elements [9,21-23]. In terms of magnetohydrodynamic modeling, the k- $\epsilon$  turbulence model is easy to solve and suitable for magnetohydrodynamic studies due to its good rate of convergence [24-29]. However, a large number of computational results and experimental data show that this approach is suitable only for simple turbulent flows, such as jet and tube flows, and is not effective for complex turbulent flows, such as strong vortices and separation. Compared to the k- $\epsilon$  model, the k- $\omega$  model is more suitable for calculating high curvature flow and internal flow. The k- $\omega$  model does not require modifying the wall function and can better describe the wall effect. Due to the relatively fewer equations used in the k- $\omega$  model, the computational efficiency is higher compared to the k- $\epsilon$  model and therefore has a faster computational speed, especially when dealing with complex flows [30]. C. Du found that the k- $\omega$  turbulence model was more accurate than the k- $\epsilon$  turbulence model for predicting turbulence by comparing the experimental results with the

calculation results of different turbulence models [31].

At present, most of the research on electromagnetic treatment of magnesium alloys has focused on the treatment of metal melts by a separate REMF or a separate PEMF, and there are fewer studies on the treatment of metal melts by a combined magnetic field; in particular, research on rotating-pulsed combined magnetic fields has not yet been reported. Therefore, this paper combines the characteristics of two stirring methods and evaluates the effects of REMF and PEMF on grain refinement and the improvement of PEMF on element segregation. The magnetic induction intensity, Lorentz force and melt velocity during the REMF, PEMF and R-PEMF treatments were analyzed via numerical simulation, which provided theoretical support for the application of electromagnetic casting technology in light metal alloys.

## 2. Model description

### 2.1. Experimental device and model establishment

The entity includes the metal melt, crucible, core, coil and air domain, where the melt size is  $\phi 32$  mm $\times$ 90 mm and  $\phi 32$  mm $\times$ 192 mm AZ91D billet ingots. Except for when the air area is divided by tetrahedral meshes, the other parts are all hexahedral meshes, as shown in Fig. 1 (a). The air area is not shown in the figure, and the physical parameters used in the numerical simulation are shown in Table 1. The pulsed electromagnetic field is caused by the waveform of the pulsed current passed inside the pulsed coil, where the number of turns of the coil is 100. The rotating magnetic field is generated by a six-pole electromagnetic stirrer, and the coils are fed with a three-phase sinusoidal alternating current with a phase difference of 120° and sequentially connected to the poles. There are 56 turns for each pole coil. Two magnetic field coils are placed on the melt axis in sequence to form a combined electromagnetic field.

The physical parameters needed for the simulation process of the stirrer model are shown in Table 1.

### 2.2. Mathematical model

In this study, the processes of magnesium alloy melt treatment in an REMF device, a PEMF device, an REMF area in an R-PEMF device and an R-PEMF device are simulated. The melt position is shown in Fig. 1(a). The effects of frequency, duty cycle and current amplitude on flow velocity under REMF and PEMF conditions were studied. The magnetic induction intensity, Lorentz force and flow field distribution of the melt in the REMF, PEMF, and REMF regions under R-PEMF and R-PEMF treatment were also studied.



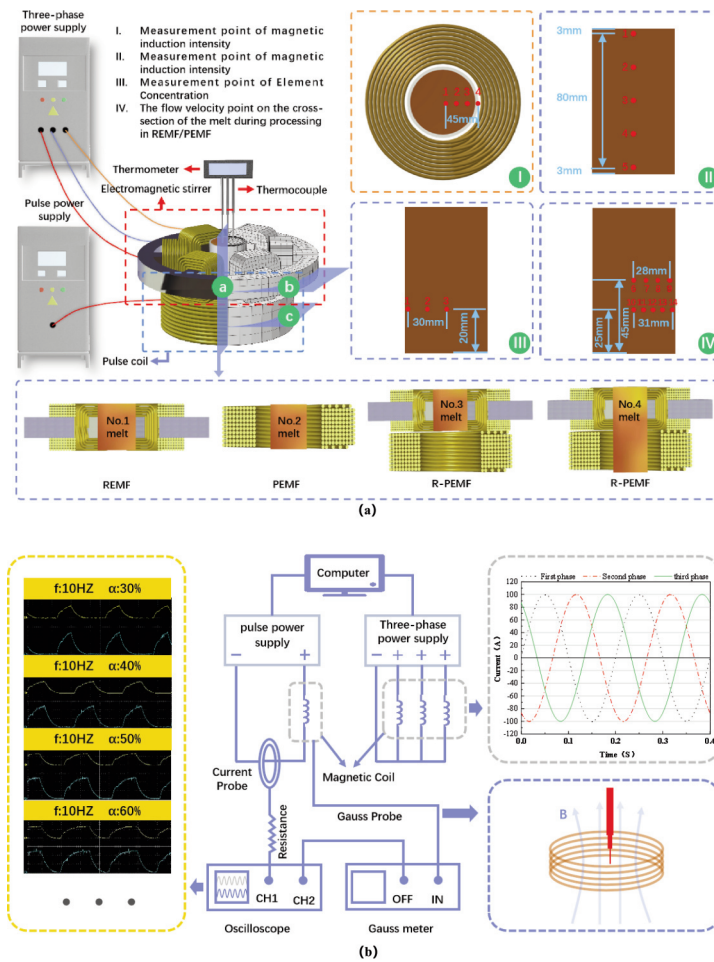


Figure 1. Schematic diagram of the electromagnetic processing system and signal feedback system; (a) Solid diagrams for the experiments and simulations; (b) Pulse, three-phase AC waveform generation and signal feedback system

2.2.1. Assumptions of the mathematical model

To facilitate the establishment of mathematical models and numerical simulation, it is necessary to simplify the model without losing rationality. Therefore, the following assumptions need to be made for the establishment of the model:

- 1) Because the stirring frequency is not high, the displacement current is not considered;
- 2) The melt is an incompressible Newtonian fluid;

- 3) The effect of free liquid level fluctuations on flow is not considered;
- 4) The relative permeability and other parameters of the slurry are scalar and do not change with time;
- 5) The Reynolds number during melt flow is very small, and the effect on the magnetic field can be neglected;
- 6) The influence of gravity on the flow field is considered.

Table 1. Material physical parameters

material	relative dielectric constant	relative permeability	electric conductivity S/m	dynamic viscosity Pa·s	density g/cm <sup>3</sup>
magnesium alloy slurry	1	1	4.9×10 <sup>6</sup>	0.0013	1.78
crucible	10	1	5000	-	2.1
silicon steel core	1	7000	1960784	-	-
copper coil	1	1	57142857	-	-
air	1	1	1	-	-



### 2.2.2. Governing equations

The governing equations of electromagnetic fields include Ampere's law, Faraday's law of electromagnetic induction, the continuity equation for magnetic flux, and Ohm's law. To obtain a definite solution, the constitutive equation needs to be added. The specific description is as follows [32,33].

Ampere's law

$$\mathbf{J} = \nabla \times \mathbf{H} \quad (1)$$

Faraday's law of electromagnetic induction

$$\nabla \times \mathbf{E} = -\frac{\partial \mathbf{B}}{\partial t} \quad (2)$$

Flux continuity equation

$$\nabla \times \mathbf{B} = 0 \quad (3)$$

Ohm's law

$$\mathbf{J} = \sigma \mathbf{E} \quad (4)$$

Constitutive equation

$$\mathbf{B} = \mu \mathbf{H} \quad (5)$$

In the above formula,  $\mathbf{B}$  is the magnetic induction (T),  $\mathbf{J}$  is the current density (A/m<sup>2</sup>),  $\mathbf{E}$  is the electric field strength (V/m),  $\mathbf{H}$  is the magnetic field strength (A/m),  $\mu$  is the relative magnetic permeability (H/m), and  $\sigma$  is the electrical conductivity (S/m).

The magnetic field calculation equation is derived from Maxwell's equations:

$$\nabla \times (\nabla \times \mathbf{B}) = -\mu \sigma \frac{\partial \mathbf{B}}{\partial t} \quad (6)$$

The interaction between the magnetic field and induced current generates the Lorentz force that drives the movement of the metal melt [33]:

$$\mathbf{F} = \mathbf{J} \times \mathbf{B} \quad (7)$$

In the formula,  $\mathbf{F}$  is the Lorentz force.

In this paper, the  $k$ - $\omega$  model is used for numerical simulation. The governing flow field equations are as follows [34]:

Momentum equation:

$$\rho(\mathbf{u} \cdot \nabla) \mathbf{u} = \nabla \cdot [-p\mathbf{I} + \mathbf{K}] + \mathbf{F} + \rho \mathbf{g} \quad (8)$$

Fluid continuous equation:

$$\rho \nabla \cdot \mathbf{u} = 0 \quad (9)$$

The viscous stress tensor or deviatoric stress tensor is given by:

$$\mathbf{K} = (\mu + \mu_T) (\nabla \mathbf{u} + (\nabla \mathbf{u})^T) \quad (10)$$

The turbulent kinetic energy  $k$  equation is:

$$\rho(\mathbf{u} \cdot \nabla) k = \nabla \cdot [(\mu + \mu_T \sigma_k^*) \nabla k] + P_k - \beta_0^* \rho \omega k \quad (11)$$

The specific dissipation rate  $\omega$  is given by

$$\rho(\mathbf{u} \cdot \nabla) \omega = \nabla \cdot [(\mu + \mu_T \sigma_\omega) \nabla \omega] + \alpha \frac{\omega}{k} P_k - \rho \beta_0 \omega^2 \quad (12)$$

Turbulent viscosity coefficient:

$$\mu_T = \rho \frac{k}{\omega} \quad (13)$$

Turbulence generation term:

$$P_k = \mu_T \left[ \nabla_{\mathbf{u}} : (\nabla_{\mathbf{u}} + (\nabla_{\mathbf{u}})^T) \right] \quad (14)$$

where  $\mathbf{u}$  is the velocity field (m/s),  $\mathbf{I}$  is the  $3 \times 3$  unit matrix,  $p$  is the pressure (Pa),  $k$  is the turbulent kinetic energy (m<sup>2</sup>/s<sup>2</sup>),  $\omega$  is the specific dissipation rate (W/mm<sup>2</sup>),  $\rho$  is the density (kg/m<sup>3</sup>), and  $\mathbf{g}$  is the acceleration of gravity (N/kg).

This numerical simulation study uses the following Wilcox constant values [35]:

$$\beta_0 = \frac{9}{125}, \beta = 5.2, \beta_0^* = \frac{9}{100}, \alpha = \frac{13}{25}, \sigma_k^* = \frac{1}{2}, \sigma_\omega = \frac{1}{2}.$$

### 2.2.3. Boundary conditions

For the magnetic field calculations, the model sets the magnetic field lines at the air domain boundary parallel to the air domain boundary and sets the outermost nodes of the air domain to be magnetically insulated. For the flow field calculation, all the boundaries of the metal melt are set to walls, and the wall conditions are set to be nonslip.

### 2.3. Model validation

The transient waveform of the magnetic induction intensity was measured by a TD8650 Gauss meter-connected oscilloscope under a PEMF of 10 Hz, a 30% duty cycle and a 100 A current amplitude. The specific testing positions are shown in Fig. 1(a) I and II, and the signal feedback and testing methods are shown in Fig. 1(b). Fig. 2 shows the comparison between the simulated and measured values, and the two results are highly consistent, with a maximum error of 3.35%. Therefore, the simulation results are considered reliable.



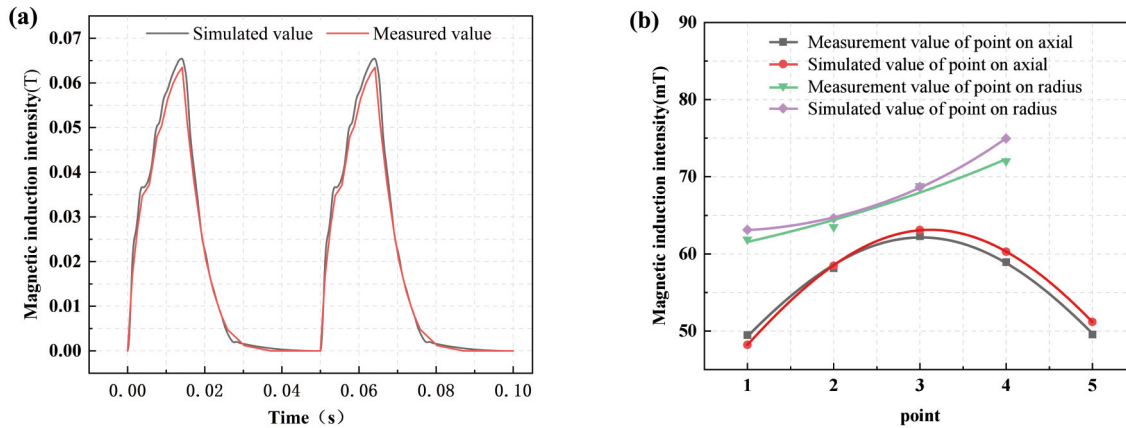


**Figure 2.** Comparison between simulation results and experimental results; a) The variation in the pulsed electromagnetic field over time; b) The variation in the peak value of the pulsed electromagnetic field with space

### 3. Results and discussion

#### 3.1. Influence of electromagnetic parameters on melt speed

Fig. 3 shows the influence of electromagnetic parameters on the melt velocity when the melt is treated by REMF and PEMF. The extraction positions of the velocity data are shown in Fig. 1 (a). Points 6-9 and 10-14 are the velocity extraction points when REMF and PEMF, respectively, treat the melt. When using a frequency of 10~40 Hz and a current of 40~100 A to treat the melt in REMF, the velocity increases with the increase of current amplitude and frequency, with the maximum velocity at 100 A and 40 Hz. However, the skin effect increases with increasing frequency, which reduces the efficiency of the rotating electromagnetic field, so it is more favorable for the Lorentz force to act on the melt core at low frequencies. When PEMF uses a frequency of 10~40 Hz and a duty cycle of 30%~60% to treat the melt, the velocity increases with the increase of frequency and reaches its maximum at 40 Hz. The maximum velocity near the edge of the melt first increases with the duty cycle and reaches its maximum at 60%. However, the maximum velocity near the center of the melt decreases first and then increases with the increase of duty cycle. PEMF has the maximum velocity when processing melt at 40 Hz and 60% duty cycle, and the frequency parameter has a greater impact on the velocity of the melt compared to the duty cycle.

#### 3.2. Laws of distribution of magnetic induction

Fig. 4 shows the magnetic field distributions of the melts treated with REMF, PEMF and R-PEMF at 0.014 s; the PEMF parameters are 10 Hz, 100 A, and 30% duty cycle, and the REMF parameters are 20 Hz and 100 A. The magnetic field direction is distributed

in the z direction when the PEMF is processed, and the magnetic field is mainly distributed in the xy plane when the REMF is processed. During R-PEMF processing, due to the superposition of two magnetic fields, the direction of the combined magnetic field has a certain inclination angle with respect to the xy plane, and the closer the area is to the PEMF coil, the greater the inclination angle.

#### 3.3. The distribution law of the Lorentz force

Fig. 5 shows the results of the Lorentz force on the No. 1 melt treated in the REMF over a variation period T. The Lorentz force distribution after 4T/8 is consistent with the change before 4T/8, and the change before 4T/8 is reproduced periodically. The Lorentz force acting on the melt exhibits a distribution with a diameter edge greater than the axis, and the maximum value is 47305 N/m<sup>3</sup>, which is mainly due to the skin effect. Second, the Lorentz forces on the upper and lower sides of the melt are greater than those in the middle. The Lorentz force acting on the cross-section of the melt shows that at each moment, the Lorentz force acting on the melt will form a pair of rotational moments with consistent directions, which will promote the rotational flow of the melt.

Fig. 6 shows the Lorentz force results for the No. 2 melt in the PEMF during a period of change. The Lorentz force on the melt also shows that the edge is greater than the axis, and the middle of the coil is greater than the upper and lower sides. The maximum Lorentz force on the melt is 21858.9 N/m<sup>3</sup>. In contrast to that in the REMF treatment, the Lorentz force on the melt during the PEMF treatment was mainly distributed perpendicular to the axial direction and periodically changed in the form of compressive stress and tensile stress.

Figure 7 shows the results of the Lorentz force on the No. 3 melt in the REMF region of R-PEMF during

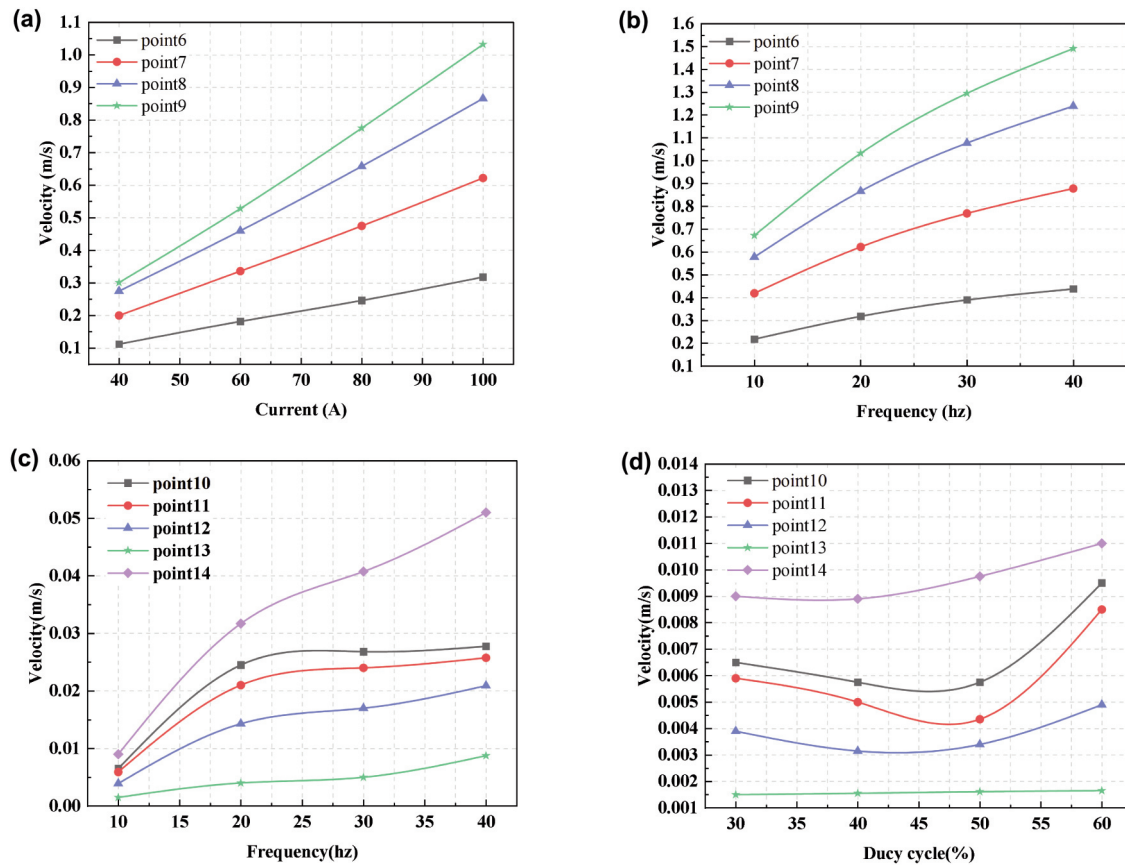


**Figure 3.** Effect of electromagnetic parameters on the melt velocity; (a) Effect of the REMF current amplitude on the melt velocity at a frequency of 20 Hz, (b) effect of the REMF frequency on the melt velocity when the current amplitude is 100 A, (c) effect of the PEMF frequency on the melt velocity when the current amplitude is 100 A and the duty cycle is 30%, and (d) effect of the PEMF duty cycle on the melt velocity when the current amplitude is 100 A and the frequency is 10 Hz

a period of change. Similarly, the Lorentz force on the melt shows a distribution in which the edge is greater than the axis, but the axial distribution is no longer present in the middle of the large ends. The Lorentz force on the melt in the cross section shown in Fig. 7(a) shows that the cross section of the No. 3 melt in the middle of the axial direction varies similarly to that in the case of the No. 1 melt treated by the REMF. Moreover, the Lorentz force on the melt at each moment in time creates a pair of rotational moments, and the directions of the moments are consistent. However, more complex asymmetric forces appear in the cross sections near the top and bottom surfaces. From the Lorentz force on the longitudinal section of the melt shown in Fig. 7 (b), it can be seen that the Lorentz force distribution on the No. 3 melt during R-PEMF treatment increases the Lorentz force in other directions in addition to the direction perpendicular to the melt central axis, which leads to the generation of secondary flow.

Fig. 8 shows the results of the Lorentz force on the No. 4 melt in R-PEMF during a period of change. Fig.

5(a) and Fig. 8(a) show that when R-PEMF treats the No. 4 melt, the Lorentz force of the melt in the REMF device area of R-PEMF is consistent with the Lorentz force when REMF treats the No. 1 melt alone, forming a pair of rotating electromagnetic moments. Fig. 6 (b) and Fig. 8 (b) show that when the melt is treated with R-PEMF, the Lorentz force of the melt in the PEMF device area is similar to that of the No. 2 melt treated with PEMF alone and changes periodically in the form of compressive stress and tensile stress. However, the Lorentz forces in the middle regions of REMF and PEMF devices are different. From the force on the cross section shown in Fig. 8 (a), it can be seen that the Lorentz moment in the middle area is no longer centered around the central axis, which will cause the rotation axis to move. It can be seen from the force on the longitudinal section that the Lorentz force parallel to the axis is generated in the middle area, as shown in Fig. 8 (b), which causes the secondary flow to affect the flow field distribution in the longitudinal section.

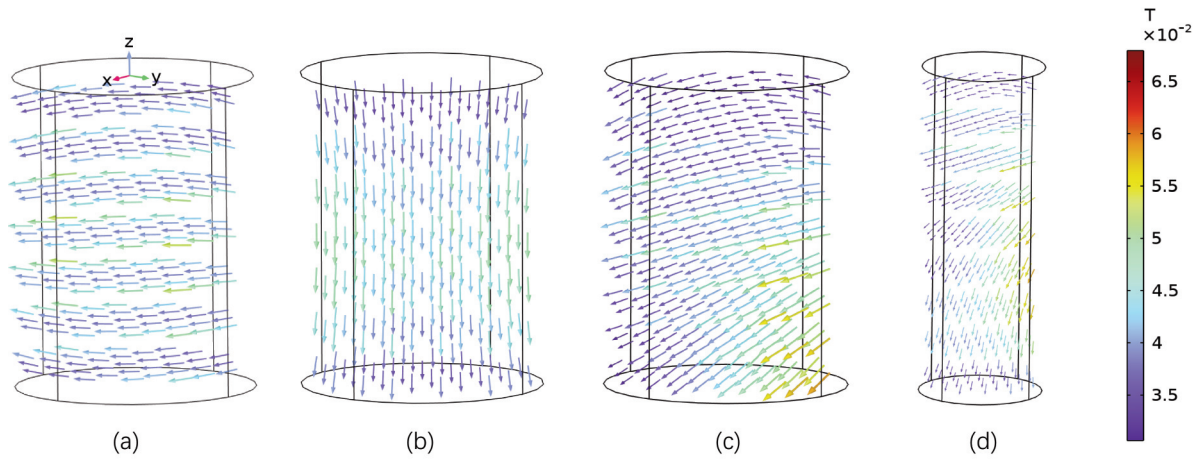


Figure 4. The magnetic field distribution of the melts treated with REMF (a), LVPM (b), the REMF region of R-PEMF (c) and R-PEMF (d) at  $t = 0.014$  s

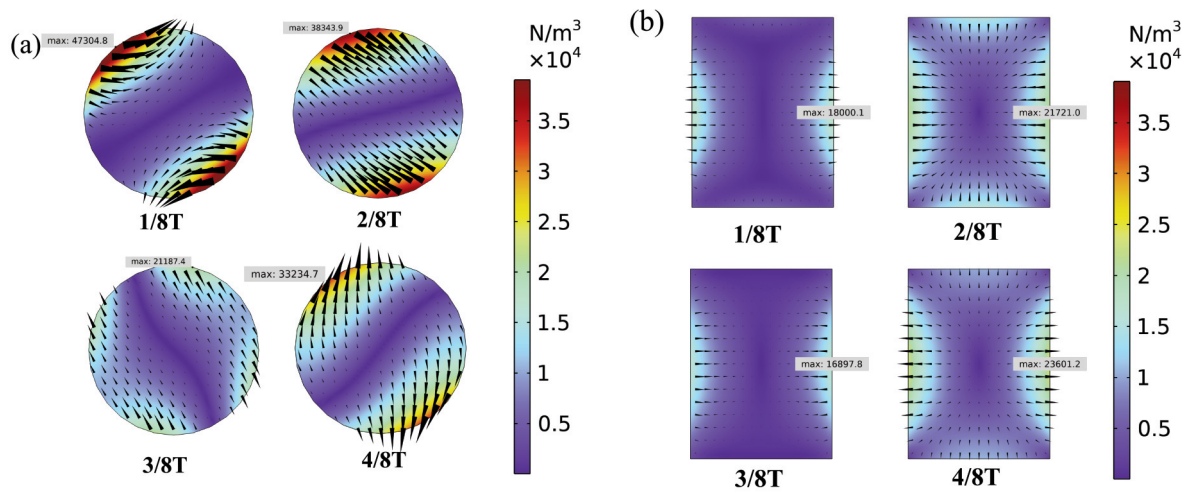


Figure 5. Lorentz force distributions of the No. 1 melt under REMF in one period; (a) Lorentz force distribution of the No. 1 melt at Section b in Fig. 1 (a); (b) Lorentz force distribution of the No. 1 melt at section an in Fig. 1 (a)

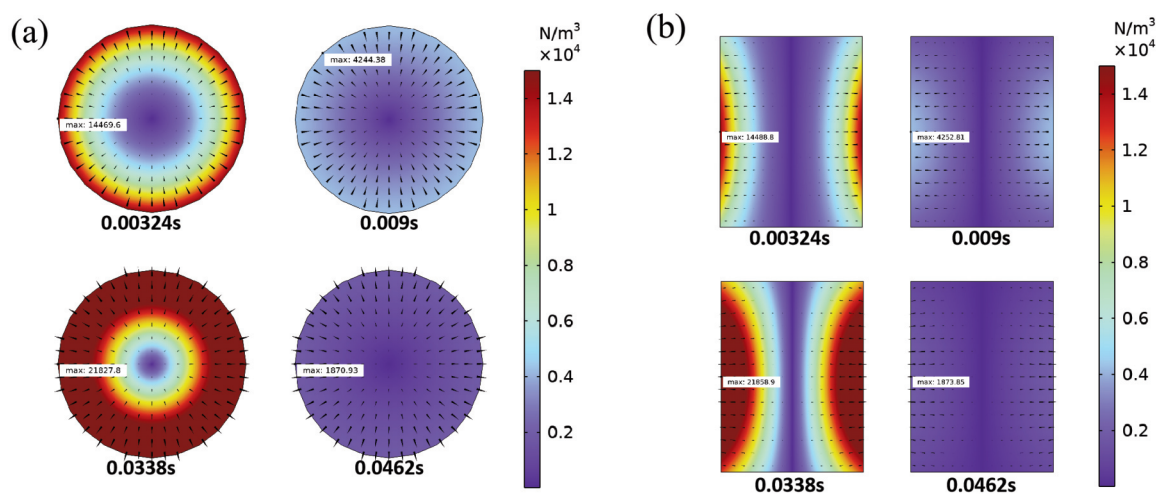
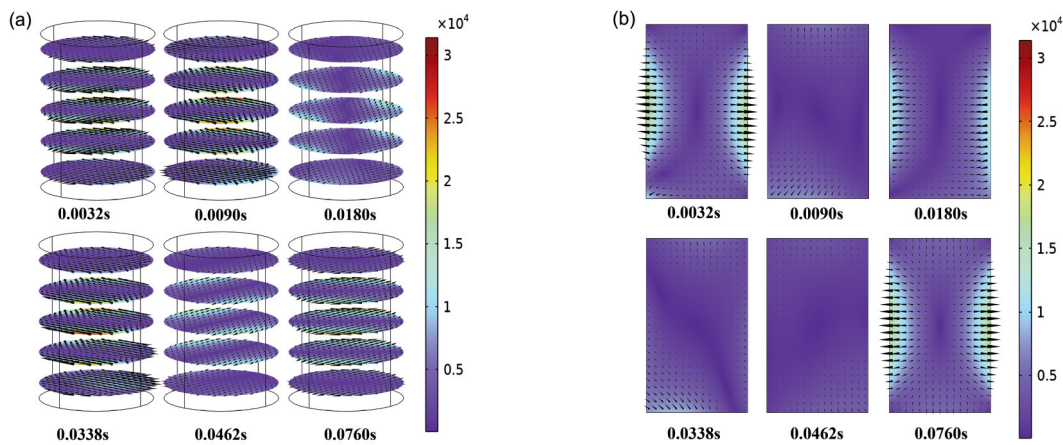
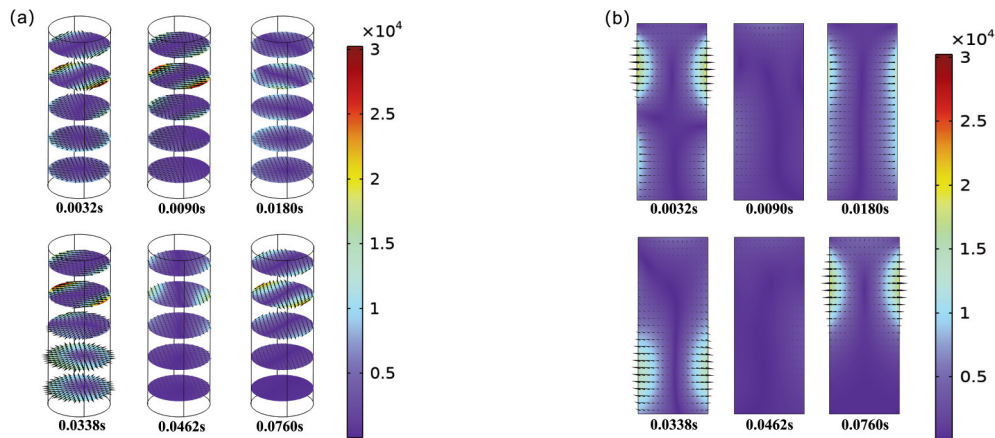


Figure 6. The Lorentz force distribution of the No. 2 melt under REMF in one period; (a) Lorentz force distribution of the No. 2 melt at cross Section c in Fig. 1 (a); (b) Lorentz force distribution of the No. 2 melt at cross section an in Fig. 1 (a)



**Figure 7.** Variation in the Lorentz force in the cross-section and longitudinal section of the No. 3 melt under REMF in one period; (a) Lorentz force distribution of the No. 3 melt in the cross-section at REMF in Fig. 1(a); (b) Lorentz force distribution of the No. 3 melt at the position of cross-section an in Fig. 1(a)



**Figure 8.** Variation in the Lorentz force in the cross-section and longitudinal section of the No. 4 melt under R-PEMF in one period; (a) Lorentz force distribution on the cross section of the No. 4 melt under R-PEMF in Fig. 1 (a); (b) Lorentz force distribution of the No. 4 melt at position an in the cross section in Figure 1 (a)

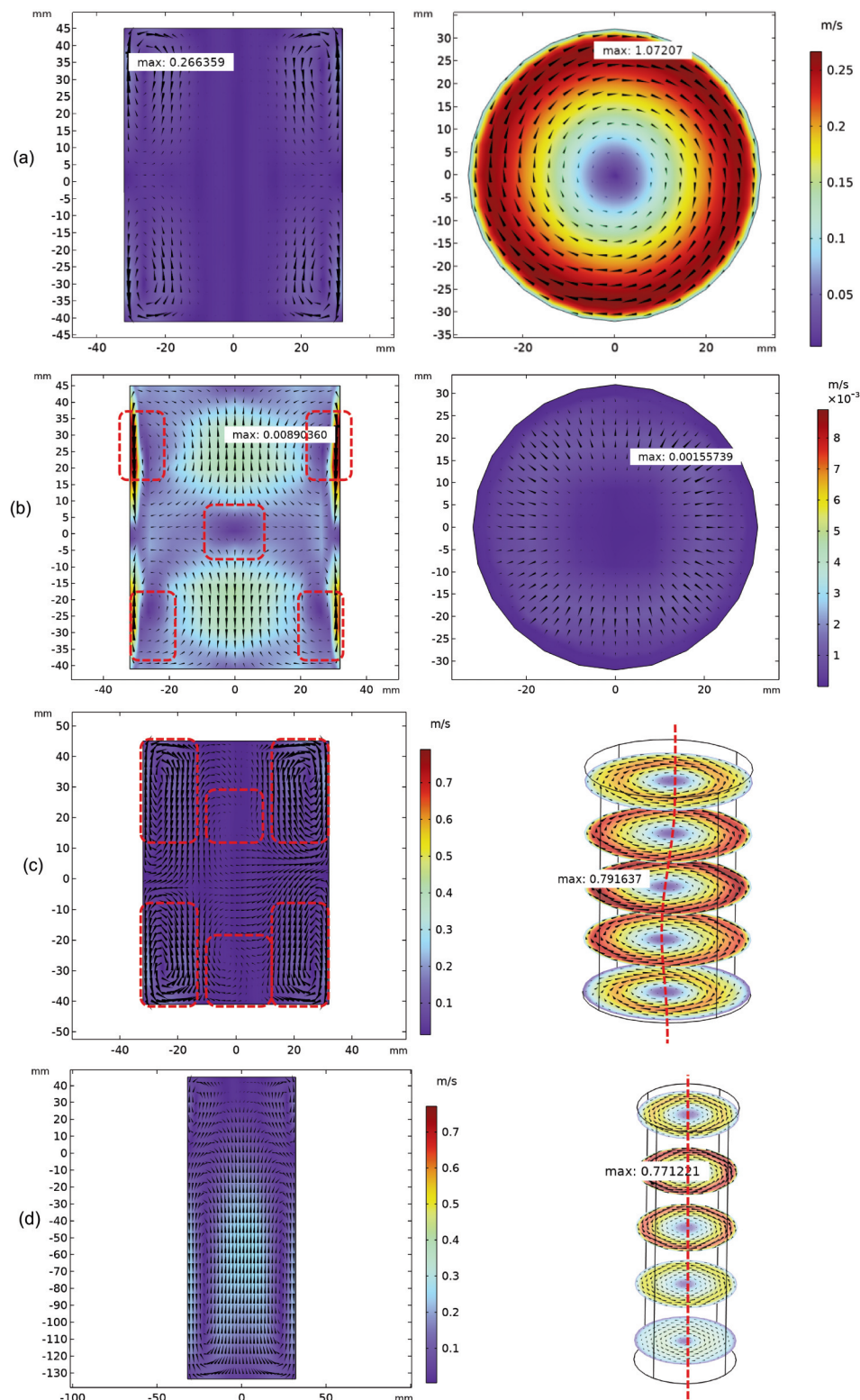
### 3.4. Flow field distribution

Fig. 9 shows the distribution of the flow field in the cross- and longitudinal sections of the melt when the melt is treated by REMF, PEMF and R-PEMF. The velocity is mainly distributed in the cross section when the melt is treated by REMF, and the velocity is mainly distributed in the longitudinal section when the melt is treated by PEMF. The situation when treating the melt in the REMF device area under R-PEMF is similar to that when treating the melt in REMF. The flow velocity is mainly distributed in the cross section and rotated along the axis, and the maximum value of the flow velocity is reduced from 1.072 m/s to 0.792 m/s. However, the axis produces a deviation from a straight line to a curve, which helps to reduce the center deviation.

In the longitudinal section, PEMF and R-PEMF produced different flow field distributions than REMF treatment. From Figure 9 (a) and Figure 9 (b), it can

be seen that the flow velocity in the middle of the longitudinal section of the melt treated by PEMF was relatively large, and there was a larger stirring range in the radial direction than in the melt treated by REMF. It can be seen from Fig. 9 (a) and Fig. 9 (c) that the radial secondary flow increased when the melt was treated in the REMF device area under R-PEMF compared with the melt treated by REMF alone, and the circulation of the flow field increased from 4 to 6. The radial stirring range is further increased, which helps to homogenize the structure. From Figure 9 (b) and Figure 9 (c), it can be seen that the flow velocity in the longitudinal section of the melt treated by the REMF device under R-PEMF is larger and the gradient of flow velocity change is smaller than that of the melt treated by PEMF alone, which will also contribute to the homogenization of the structure.

The fluid morphology of the No. 4 melt treated with R-PEMF in the transition region between the rotating and the pulse device was analyzed, as shown



**Figure 9.** Distribution pattern of flow field under different magnetic fields; (a) Velocity in the longitudinal and transverse sections of No.1 melt when treated under REMF in Fig. 1(a); (b) Velocity in the longitudinal and transverse section of No.2 melt when treated under PEMF in Fig. 1(a); (c) Velocity in the longitudinal and transverse section when No.3 melt is treated under R-PEMF (REMF region) in Fig. 1(a); (d) Velocity in the longitudinal and transverse sections of No.4 melt when treated under R-PEMF in Fig. 1(a)

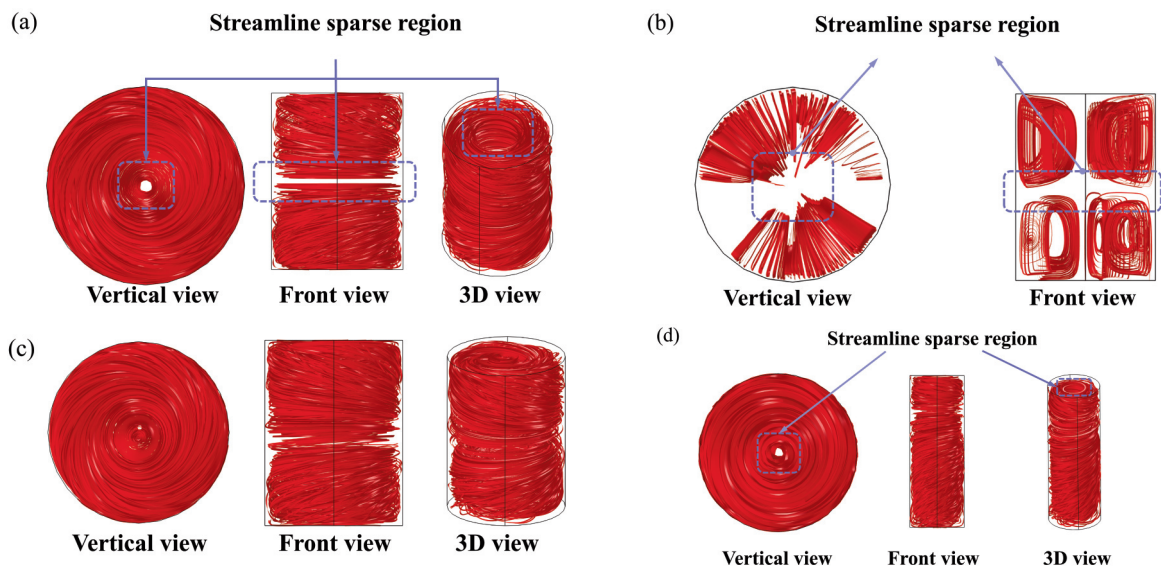
in Figure 9 (d). The maximum flow velocity appears in the cross section, and the maximum value is further reduced to 0.771 m/s. From Fig. 9(c) and Fig. 9(d), the axis of rotation returns from a curve to a straight line when the melt is treated under R-PEMF. In addition, the distribution area of the radial secondary flow is reduced when the melt is processed under R-PEMF and is mainly concentrated near the area of the REMF device. This weakens the effect of R-PEMF on reducing the central segregation of the melt compared to the case where the melt is treated in the REMF device region under R-PEMF.

Fig. 10 shows the streamline distribution of the melt in the REMF treatment, PEMF treatment and R-PEMF treatment. Fig. 10 (a) shows that the melt mainly rotates in the circumferential direction when REMF treats the No. 1 melt, and the streamlines are mainly distributed at the edge and are layered at the upper and lower parts of the melt, representing little melt exchange between the upper and lower parts of

as shown in Fig. 10 (c). When the No. 4 melt is treated in R-PEMF, the streamlines are more evenly distributed in the axial direction, which further strengthens the exchange of upper and lower fluids. However, the streamline at the axis has been reduced to a certain extent, which weakens the stirring effect of R-PEMF at reducing the melt axis.

### 3.5. Experimental study on solidification

The solidification experiment used the AZ91D alloy as the research object. The AZ91D magnesium alloy was heated to 700 °C and melted for 10 min. Then, the crucible was removed, and the surface oxide film was removed by a slag scoop and cast into the crucible for electromagnetic treatment until the sample was completely solidified. During the process, SF<sub>6</sub> gas was used to protect the upper part of the crucible to prevent the oxidation of the magnesium alloy. The frequency parameter of REMF is 20 Hz, the



**Figure 10.** The streamline distribution of melts under different magnetic field treatment conditions; (a) The streamline distribution of the No. 1 melt under REMF treatment in Fig. 1 (a); (b) The streamline distribution of the No. 2 melt under PEMF treatment in Fig. 1 (a); (c) The streamline distribution of the No. 3 melt under the R-PEMF (REMF region) treatment in Fig. 1 (a); (d) Streamline distribution of the No. 4 melt under the R-PEMF treatment in Fig. 1 (a)

the melt. Fig. 10 (b) shows that when the PEMF treats the No. 2 melt, the melt mainly rotates in the axial direction, and the upper and lower parts of the melt are layered, resulting in little exchange between the upper and lower parts of the melt. However, when the No. 3 melt is treated in the REMF region of R-PEMF, the streamlines are no longer distributed mainly at the edge of the melt, which is beneficial for reducing segregation at the axis. In addition, the upper and lower parts of the melt strengthen the melt exchange, which facilitates the homogenization of the structure,

frequency parameter of PEMF is 10 Hz, the duty cycle is 30%, and the current amplitude of REMF and PEMF is set to 100 A. After the ingot was cooled, the sample was cut along the longitudinal section from the middle, after which the sample was polished. The samples were etched with acetic acid for 4 s and then washed with deionized water immediately, after which the microstructure was observed immediately. Finally, samples were taken at points 1, 2 and 3 in Fig. 1(a)-III, and the elemental contents of Al (The maximum measurement error is 0.485%), Zn (The

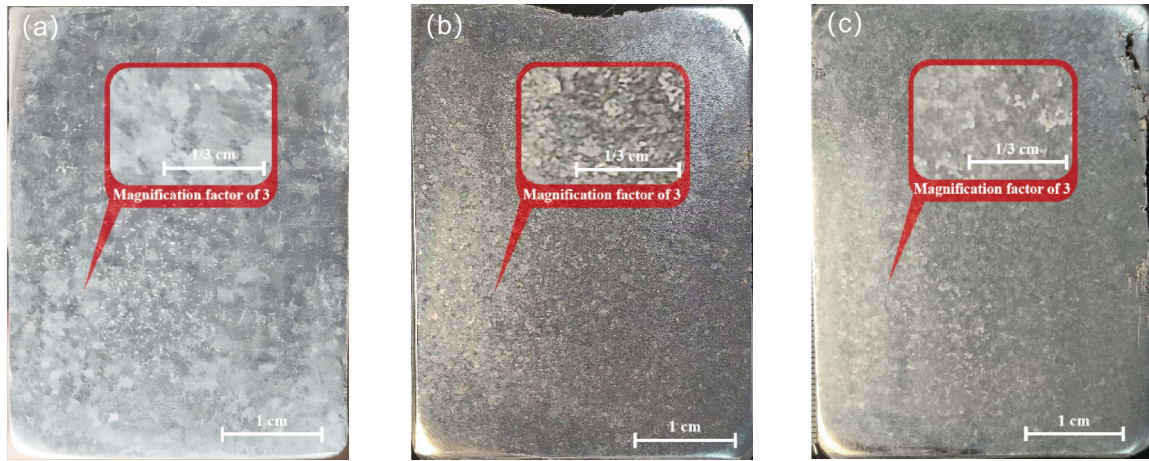


**Figure 11.** The cross section of the melt after different magnetic field treatments; (a) Cross section of the melt in the absence of magnetic field solidification; (b) Cross section of the melt treated by REMF; (c) Cross-sections of melts treated with R-PEMF (REMF region)

maximum measurement error is 0.05%), and Mn (The maximum measurement error is 0.025%) in the specimens were measured via ICP.

Figure 11 shows the longitudinal section surface of the AZ91D magnesium alloy without magnetic field solidification, after REMF treatment and after REMF region treatment in R-PEMF. The grains of the AZ91D magnesium alloy were effectively homogenized and refined after the REMF treatment and after the REMF region in R-PEMF.

In order to compare the segregation of elements under different solidification conditions, the relative deviations of Al, Zn, and Mn element concentrations between points 1 and 2, as well as points 1 and 3, were calculated using formulas  $|x_{12}| = \left| \frac{c_1 - c_2}{c_1} \right|$  and  $|x_{13}| = \left| \frac{c_1 - c_3}{c_1} \right|$  after obtaining the ICP element content results. The mean square deviation of the distribution of each element was calculated using formula where  $s = \sqrt{s^2} = \sqrt{\frac{\sum_{i=1}^n (c_i - \bar{c})^2}{n}}$

$|x|$  represents the relative deviation,  $C_n$  represents the element concentration at point n,  $s$  represents the mean square deviation of element distribution,  $\bar{c}$  is the average value of element content

at all sampling points, and n is the total number of sampling points. The results are shown in Table 2. Compared with the ingot without magnetic field solidification, the Al in the ingot after REMF treatment had greater segregation, and the segregation after REMF treatment in R-PEMF was reduced to the minimum value under the three different treatment conditions, which improved the homogenization degree of the Al. In contrast, the segregation degree of Mn is aggravated after the melt is treated in the REMF region of R-PEMF.

The presence of secondary flow in the melt flow field causes sufficient stirring of the melt and leads to a homogenization of temperature and solute composition. On the one hand, the solidification equilibrium temperature increases under the electromagnetic field, and the number of primary crystal nuclei increases, resulting in grain refinement [36, 37]. On the other hand, due to the intensification of momentum transfer, the solid-liquid two-phase region cannot exist in equilibrium, which suppresses crystal growth [38]. However, due to the significant impact of different electromagnetic process

**Table 2.** Elemental segregation

elemental	solidification condition	point1-2 relative deviation	point1-3 relative deviation	Mean square deviation
Al	No magnetic field	0.66% —	3.81% —	0.0012469
	REMF	5.58% ↑	7.86% ↑	0.002502
	R-PEMF	0.25% ↓	3.36% ↓	0.0012122
	(REMF region)			
Zn	No magnetic field	2.01% —	8.71% —	0.0001113
	REMF	3.13% ↑	8.25% ↓	0.0001066
	R-PEMF (REMF region)	5.18% ↑	6.95% ↓	0.0000942
Mn	No magnetic field	0.51% —	1.19% —	0.0000096
	REMF	0.76% ↑	0.63% ↓	0.0000044
	R-PEMF (REMF region)	5.00% ↑	6.30% ↑	0.0000370

parameters on segregation and crystal growth, the coupling research between electromagnetic field process and solidification process will be further conducted to obtain high quality microstructure, which is suitable for different element and geometric ingots.

#### 4. Conclusion

In this study, the processes of treatment of AZ91D magnesium alloy in the REMF, PEMF, and REMF regions under R-PEMF and R-PEMF conditions were simulated by creating corresponding three-dimensional models. The magnetic field and flow field characteristics during the casting process of magnesium alloys under different magnetic fields were investigated. The results obtained are as follows:

For the magnesium alloy melt, the velocity increases with increasing current amplitude and frequency during the REMF treatment, and the highest velocity occurs at 100 A and 40 Hz. The PEMF has the highest velocity at 40 Hz and a 60% duty cycle.

The Lorentz force of the melt during the REMF treatment is mainly manifested as a rotational force in the circumferential direction on the cross-section. The Lorentz force of the melt during PEMF treatment is mainly characterized by periodic changes in extrusion force and tension. When the melt is treated in the R-PEMF in the REMF region and in the R-PEMF region, the Lorentz force in the cross-section is mainly manifested as a rotational force in the circumferential direction, but there is also a force that is not perpendicular to the axis.

The flow field distribution in the REMF region of R-PEMF differs from that in the REMF and PEMF magnetic fields. A radial secondary flow is generated, which increases the stirring area of the melt, reduces the velocity gradient, bends the axis of rotation and increases the exchange of the upper and lower parts of the melt, which helps to reduce center segregation and improve microstructural uniformity. However, when the melt is treated with R-PEMF, the velocity axis of the flow field returns to a straight line, which weakens the stirring effect of the reduced R-PEMF on the melt center.

#### Acknowledgment

*This work is supported by the Inner Mongolia Autonomous Region Science and Technology Program (Project Number: 2021GG0095) and the Inner Mongolia Autonomous Region Science and Technology Program (Project Number: 2022YFHH0094).*

#### Author contributions

*Zhong Liang: Conceptualization, Methodology, Software, Writing, Original Draft*

*Qingwei Bai: Writing, Review & Editing*

*Yingchun Tian, Yang Liu, Kaihua Zhang, Haomin*

*Lai: Visualization*

#### Data Availability Statement

*Data will be made available on request.*

#### Conflicts of Interest

*The authors declare no conflict of interest.*

#### References

- [1] K. Kubota, M. Mabuchi, K. Higashi, Review processing and mechanical properties of fine-grained magnesium alloys, *Journal of Materials Science*, 34 (1999) 2255–2262. <https://doi.org/10.1023/A:1004561205627>
- [2] Y. Ali, D. Qiu, B. Jiang, F. Pan, M. Zhang, Current research progress in grain refinement of cast magnesium alloys: A review article, *Journal of Alloys and Compounds*, 619 (2015) 639–651. <https://doi.org/10.1016/j.jallcom.2014.09.061>
- [3] A. Atrens, G. Song, M. Liu, Z. Shi, F. Cao, M. Dargusch, Review of recent developments in the field of magnesium corrosion, *Advanced Engineering Materials*, 17 (4) (2015) 400–453. <https://doi.org/10.1002/adem.201400434>
- [4] M. Easton, A. Beer, M. Barnett, C. Davies, G. Dunlop, Y. Durandet, S. Blacket, T. Hilditch, P. Beggs, Magnesium alloy applications in automotive structures, *JOM*, 60 (11) (2008) 57–62. <https://doi.org/10.1007/s11837-008-0150-8>
- [5] Z. Kang, W. Li, Facile and fast fabrication of superhydrophobic surface on magnesium alloy by one-step electrodeposition method, *Journal of Industrial and Engineering Chemistry*, 50 (2017) 50–56. <https://doi.org/10.1016/j.jiec.2017.01.016>
- [6] M. Kulekci, Magnesium and its alloys applications in automotive industry, *The International Journal of Advanced Manufacturing Technology*, 39 (9) (2008) 851–865. <https://doi.org/10.1007/s00170-007-1279-2>
- [7] M. La, H. Zhou, N. Li, Y. Xin, R. Sha, S. Bao, P. Jin, Improved performance of Mg–Y alloy thin film switchable mirrors after coating with a superhydrophobic surface, *Applied Surface Science*, 403 (2017) 23–28. <https://doi.org/10.1016/j.apsusc.2017.01.106>
- [8] A. Dahle, Y. Lee, M. Nave, P. Schaffer, D. StJohn, Development of the as-cast microstructure in magnesium–aluminium alloys, *Journal of Light Metals*, 1 (1) (2001) 61–72. [https://doi.org/10.1016/S1471-5317\(00\)00007-9](https://doi.org/10.1016/S1471-5317(00)00007-9)
- [9] W. Duan, Y. Yang, W. Liu, Z. Zhang, J. Cui, Modelling the fluid flow, solidification and segregation behavior in electromagnetic DC casting of magnesium alloy, *Simulation Modelling Practice and Theory*, 115 (2022) 102460. <https://doi.org/10.1016/j.simpat.2021.102460>



- [10] X. Tong, G. You, Y. Wang, H. Wu, W. Liu, P. Li, W. Guo, Effect of ultrasonic treatment on segregation and mechanical properties of as-cast Mg–Gd binary alloys, *Materials Science and Engineering: A*, 731 (2018) 44–53. <https://doi.org/10.1016/j.msea.2018.06.017>
- [11] X. Tong, G. You, F. Yao, M. Ebrahimi, X. Deng, S. Attarilar, Segregation behavior and its regulating process in as-cast magnesium alloy containing heavy rare earth, *Journal of Rare Earths*, 40 (8) (2022) 1291–1304. <https://doi.org/10.1016/j.jre.2021.08.009>
- [12] M. Li, M. Sun, L. Meng, X. Guo, Quasi-in situ immersion characterization of grain structures evolution revealing the corrosion resistance of Al-Zn-Mg alloys with various Sc additions, *Journal of Central South University*, 30 (12) (2023) 3964–3974. <https://doi.org/10.1007/s11771-023-5491-5>
- [13] H. Shao, Y. Huang, Y. Wang, Effect of ageing process on microstructure, corrosion behaviors and mechanical properties of Al-5.6Zn-1.6Mg-0.05Zr alloy, *Journal of Central South University*, 29 (3) (2022) 1029–1040. <https://doi.org/10.1007/s11771-022-4953-5>
- [14] E. Karakulak, A review: Past, present and future of grain refining of magnesium castings, *Journal of Magnesium and Alloys*, 7 (3) (2019) 355–369. <https://doi.org/10.1016/j.jma.2019.05.001>
- [15] I. Tzanakis, G. Lebon, D. Eskin, K. Pericleous, Investigation of the factors influencing cavitation intensity during the ultrasonic treatment of molten aluminium, *Materials & Design*, 90 (2016) 979–983. <https://doi.org/10.1016/j.matdes.2015.11.010>
- [16] S. Gao, Q. Le, Z. Zhang, J. Cui, Grain refinement of AZ31 magnesium alloy by electromagnetic stirring under effect of grain-refiner, *Bulletin of Materials Science*, 35 (4) (2012) 651–655. <https://doi.org/10.1007/s12034-012-0345-z>
- [17] W. Mao, Z. Zheng, H. Cheng, Microstructures of AZ91D alloy solidified during electromagnetic stirring, *Transactions of Nonferrous Metals Society of China*, 15 (1) (2005) 72–76.
- [18] J. Fu, Y. Yang, Microstructure and mechanical properties of Mg–Al–Zn alloy under a low-voltage pulsed magnetic field, *Materials Letters*, 67 (1) (2012) 252–255. <https://doi.org/10.1016/j.matlet.2011.09.021>
- [19] W. Griffiths, D. McCartney, The effect of electromagnetic stirring on macrostructure and macrosegregation in the aluminium alloy 7150, *Materials Science and Engineering: A*, 222 (2) (1997) 140–148. [https://doi.org/10.1016/S0921-5093\(96\)10527-X](https://doi.org/10.1016/S0921-5093(96)10527-X)
- [20] C. Zhang, S. Xu, W. Tang, Y. Xie, Effect of Electromagnetic Stirring on the Macro-segregation in Magnesium Alloy Ingots, *Shanghai Metals*, 39 (5) (2017) 4.
- [21] S. Guo, Q. Le, Y. Han, Z. Zhao, J. Cui, The effect of the electromagnetic vibration on the microstructure, segregation, and mechanical properties of As-cast AZ80 magnesium alloy billet, *Metallurgical and Materials Transactions A*, 37 (12) (2006) 3715–3724. <https://doi.org/10.1007/s11661-006-1065-z>
- [22] W. Bin, Y. Y. Sheng, M. Xiaoping, T. Wenhui, Simulation of electromagnetic-flow fields in Mg melt under pulsed magnetic field, *Transactions of Nonferrous Metals Society of China*, 20 (2) (2010) 283–288. [https://doi.org/10.1016/S1003-6326\(09\)60135-7](https://doi.org/10.1016/S1003-6326(09)60135-7)
- [23] W. Duan, S. Yin, W. Liu, Z. Zhao, K. Hu, P. Wang, J. Cui, Z. Zhang, Numerical and experimental studies on solidification of AZ80 magnesium alloy under out-of-phase pulsed magnetic field, *Journal of Magnesium and Alloys*, 9 (1) (2021) 166–182. <https://doi.org/10.1016/j.jma.2020.03.008>
- [24] Q. Dong, J. Zhang, Q. Liu, Y. Yin, Magneto-hydrodynamic calculation for electromagnetic stirring coupling fluid flow and solidification in continuously cast billets, *Steel Research International*, 88 (11) (2017) 1700067. <https://doi.org/10.1002/srin.201700067>
- [25] H. Liu, M. Xu, S. Qiu, H. Zhang, Numerical Simulation of Fluid Flow in a Round Bloom Mold with In-Mold Rotary Electromagnetic Stirring, *Metallurgical and Materials Transactions B*, 43 (6) (2012) 1657–1675. <https://doi.org/10.1007/s11663-012-9737-0>
- [26] T. Natarajan, N. El-Kaddah, Finite element analysis of electromagnetic and fluid flow phenomena in rotary electromagnetic stirring of steel, *Applied Mathematical Modelling*, 28 (1) (2004) 47–61. [https://doi.org/10.1016/S0307-904X\(03\)00114-8](https://doi.org/10.1016/S0307-904X(03)00114-8)
- [27] B. Ren, D. Chen, H. Wang, M. Long, Z. Han, Numerical simulation of fluid flow and solidification in bloom continuous casting mould with electromagnetic stirring, *Ironmaking & Steelmaking*, 42 (6) (2015) 401–408. <https://doi.org/10.1179/1743281214Y.0000000240>
- [28] B. Wang, W. Chen, Y. Chen, Y. Feng, Coupled numerical simulation on electromagnetic field and flow field in the round billet mould with electromagnetic stirring, *Ironmaking & Steelmaking*, 42 (1) (2015) 63–69. <https://doi.org/10.1179/1743281214Y.0000000201>
- [29] Z. Rui, W. JunJie, Z. YunHu, T. Zhichao, M. Shencheng, Z. QiJie, Flow and Solidification Structure in Metal Melts driven by a Combined Magnetic Field, *Acta Metallurgica Sinica*, 60 (02) (2024) 231–246. <https://doi.org/10.11900/0412.1961.2022.00032>
- [30] B. Yang, A. Deng, Y. Li, X. Xu, E. Wang, Numerical simulation of flow and solidification in continuous casting process with mold electromagnetic stirring, *Journal of Iron and Steel Research International*, 26 (3) (2019) 219–229. <https://doi.org/10.1007/s42243-018-0162-8>
- [31] C. Du, L. Li, X. Wu, Z. Feng, Effect of jet nozzle geometry on flow and heat transfer performance of vortex cooling for gas turbine blade leading edge, *Applied Thermal Engineering*, 93 (2016) 1020–1032. <https://doi.org/10.1016/j.applthermaleng.2015.09.087>
- [32] K. Spitzer, Application of rotating magnetic fields in Czochralski crystal growth, *Progress in Crystal Growth and Characterization of Materials*, 38 (1-4) (1999) 59–71. [https://doi.org/10.1016/S0960-8974\(99\)00008-X](https://doi.org/10.1016/S0960-8974(99)00008-X)
- [33] L. Guidong, M. Yonglin, X. Shuqing, B. Xinyu, B. Qingwei, Numerical Simulation of Electromagnetic Field and Flow Field in Square Wave Electromagnetic Stirring of Continuous Casting Mould, *Foundry Technology*, 40 (03) (2019) 276–282.
- [34] W. David C, *Turbulence Modeling for CFD (Third Edition) (Hardcover)*, DCW Industries, La Canada, 2006, 332-334.
- [35] D. Kuzmin, O. Mierka, S. Turek, On the implementation of the  $\kappa$ - $\epsilon$  turbulence model in incompressible flow solvers based on a finite element discretisation, *International Journal of Computing Science and Mathematics*, 1 (2-4) (2007) 193–206.



- <https://doi.org/10.1504/IJCSM.2007.016531>
- [36] B. Qingwei, M. Yonglin, X. Shuqing, F. Yanfei, B. Xinyu, C. Zhongyi, Solidified Microstructure Evolution of 7A04 Alloy Under Surface Electromagnetic Pulse Treatment, *Materials Review*, 32 (12) (2018) 2021–2027.
- [37] H. Lai, Q. Bai, Y. Tian, P. Xu, Z. Liang, X. Liu, Effect of Pulsed Magnetic Field on Solidification Microstructure and Properties of Rare Earth AZ91D Magnesium Alloy, *Zhuzao(Foundry)*, 73 (01) (2024) 68–75.
- [38] E. Liotti, A. Lui, R. Vincent, S. Kumar, Z. Guo, T. Connolly, I. Dolbnya, M. Hart, L. Arnberg, R. Mathiesen, P. Grant, A synchrotron X-ray radiography study of dendrite fragmentation induced by a pulsed electromagnetic field in an Al–15Cu alloy, *Acta Materialia*, 70 (2014) 228–239.  
<https://doi.org/10.1016/j.actamat.2014.02.024>

## NUMERIČKA SIMULACIJA PROCESA LIVENJA LEGURE MAGNEZIJUMA AZ91D POD KOMBINOVANIM ROTACIONO-PULSIRAJUĆIM ELEKTROMAGNETNIM POLJEM

Z. Liang <sup>a</sup>, Q.-W. Bai <sup>abc\*</sup>, Y.-C. Tian <sup>d</sup>, Y. Liu <sup>a</sup>, K.-H. Zhang <sup>a</sup>, H.-M. Lai <sup>a</sup>

<sup>a</sup> Fakultet za industriju retkih metala, Univerzitet za nauku i tehnologiju Unutrašnje Mongolije, Baotou, Kina

<sup>b</sup> Glavna laboratorija za zelenu ekstrakciju i efikasnu upotrebu resursa retkih metala (Univerzitet za nauku i tehnologiju Unutrašnje Mongolije), Ministarstvo prosvete, Baotou, Kina

<sup>c</sup> Centar za inovacije o karbonskoj neutralnosti Autonomne regije Unutrašnje Mongolije

<sup>d</sup> Institut za metalne materijale Unutrašnje Mongolije, Baotou, Narodna Republika Kina

### Apstrakt

Koristeći leguru magnezijuma AZ91D kao istraživački objekat, kreiran je i simuliran trodimenzionalni (3D) numerički model pomoću softvera za simulacionu analizu. Ispitivani su efekti rotacionog elektromagnetnog polja (REMF), pulsirajućeg elektromagnetnog polja (PEMF) i rotaciono-pulsirajućeg elektromagnetnog polja (R-PEMF) na magnetno polje i tok metalnog rastopa. Rezultati simulacije pokazuju da se tokom REMF tretmana generiše rotaciona sila na poprečnom preseku rastopa, dok PEMF deluje sa magnetnim pritiskom na poprečni presek rastopa. Pod kombinovanim delovanjem ovih sila, Lorencova sila se povećava paralelno sa osom rastopa, a sekundarni tok usmeren ka jezgu rastopa se generiše, što doprinosi homogenizaciji rastopa. Analizom strukture očvršćavanja i raspodele elemenata u metalu, pokazano je da R-PEMF efikasno poboljšava strukturu očvršćavanja i makrosegregaciju aluminijuma u leguri magnezijuma AZ91D.

**Ključne reči:** Pulsirajuće elektromagnetno polje; Rotaciono elektromagnetno polje; Kombinovano elektromagnetno polje; Legura magnezijuma; Numerička simulacija

